metals

MDPI

Article

New Insights into the Ingot Breakdown Mechanism of Near-β Titanium Alloy: An Orientation-Driven Perspective

Xianghong Liu [1,2,*], Tao Wang [2,3,*], Xiaolong Ren [2,3], Jie Fu [2,3], Liang Cheng [4,5], Bin Zhu [5] and Kaixuan Wang [2,3]

1 Northwest Institute for Non-Ferrous Metal Research, Xi'an 710016, China
2 National & Local Joint Engineering Laboratory for Special Titanium Alloy Processing Technology, Xi'an 710018, China; renxiaolong32@163.com (X.R.); shanxifujie@c-wst.com (J.F.); kingsin@c-wst.com (K.W.)
3 Western Superconducting Technologies Co., Ltd., Xi'an 710018, China
4 Innovation Center, NPU·Chongqing, Chongqing 401135, China; chengliang525@163.com
5 School of Materials and Engineering, Jiangsu University of Technology, Changzhou 213001, China; zhubin@jsut.edu.cn
* Correspondence: xhliu@c-wst.com (X.L.); wang_tao@c-wst.com (T.W.)

Abstract: The ingot breakdown behavior of a typical near-β titanium alloy, Ti-55511, was investigated by various multi-pass upsetting processes. Particular emphasis was placed on the breakdown mechanism of the ultra-large β grains. The results showed that the upsetting far above the β-transus yielded uniform and refined macrostructure with relatively coarse grain size. In contrast, subtransus deformation within the (α + β) dual-phase field caused severe strain localization and macroscale shear bands. It was found that the static recrystallization during the post-deformation annealing was determined by the preferential grain orientations, which were closely related to the processing conditions. During β-working, the stable <001>-oriented grains were predominant and fragmentized mainly via a so-called "low-angle grain boundary merging" mechanism, even under a fairly low deformation. However, the vast <001> grain area was unbeneficial for microstructural conversion since it provided minor nucleation sites for the subsequent annealing. In contrast, the α/β-working produced the majority <111>-orientated grains, which were strongly inclined to strain localization. Highly misoriented deformation/shear bands were massively produced within the <111> grains, providing abundant nucleation sites for static recrystallization and, hence, were favorable for microstructural refinement. Furthermore, the intrinsic causes for deformation nonuniformity were discussed in detail, as well as the competition between microstructural homogeneity and refinement.

Keywords: titanium alloys; hot working; recrystallization; texture; grain refinement

check for updates

Citation: Liu, X.; Wang, T.; Ren, X.; Fu, J.; Cheng, L.; Zhu, B.; Wang, K. New Insights into the Ingot Breakdown Mechanism of Near-β Titanium Alloy: An Orientation-Driven Perspective. *Metals* **2024**, *14*, 792. https://doi.org/10.3390/met14070792

Academic Editor: Antonio Mateo

Received: 10 June 2024
Revised: 2 July 2024
Accepted: 5 July 2024
Published: 7 July 2024

Copyright: © 2024 by the authors. Licensee MDPI, Basel, Switzerland. This article is an open access article distributed under the terms and conditions of the Creative Commons Attribution (CC BY) license (https://creativecommons.org/licenses/by/4.0/).

1. Introduction

The so-called near-β titanium alloys, which are enriched in β-stabilizer such as Mo, Cr, V, and Fe, have superior workability and good corrosion resistance, together with a good combination of high strength, ductility, and fatigue strength [1,2]. Hence, they have been widely utilized in the production of lightweight components for aircraft [3,4]. To meet the stringent service requirements on mechanical properties, the near-β titanium alloys have to undergo multi-pass thermomechanical processing to accurately control the microstructure [5]. Thereinto, the primary hot working plays a crucial role in the ingot breakdown, which provides a desired fine-grained basis for further processing. The phenomenology and mechanisms underlying the microstructure conversion during the primary hot working of near-β titanium alloys have received considerable attention in the past decades, and a number of insightful reviews have arisen [5–7]. Through a rough survey of the related literature, one can draw some common features with respect to the microstructural refinement for various near-β titanium alloys.

In general, the primary hot working can be performed within the pure β-phase field (β-working) and/or in the (α+β) dual-phase field (α/β-working) [7]. During β-working,

the deformation is thought to be typical of materials undergoing dynamic recovery (DRV) due to the high stacking-fault energy of the β-phase [8]. This leads to the gradual flattening or elongation of the prior β grains, combined with the generation of numerous subgrains whose dimensions are decided by the processing parameters. During further straining, the misorientation of the sub-boundaries is gradually increased in a homogeneous manner, eventually leading to the complete fragmentation of the β-matrix after sufficient cumulated strain [9]. This is known as the continuous dynamic recrystallization (CDRX) [10]. Unlike in a classical statically recrystallized (SRX) material, high angle boundaries (HAGBs) in such a CDRXed structure cannot systematically close up around grains even under extremely large strain (~14) for near-β titanium alloys [11]. Meanwhile, some investigations suggested that DRX also occurs in the vicinity of the β GBs, forming a necklace structure analogous to that produced by the traditional discontinuous DRX (DDRX) [8,12,13]. Also, the DRX can either occur through a geometrical manner, which is characterized by the local pinching off and fragmentation of the elongated grains [13] or nucleate at deformation/shear bands [9,12,14]. The case is more complicated for α/β-working. Due to the complicated interaction between α and β-phases [15], the α-phase shows a more equiaxed morphology due to DRX as well as thermomechanical-induced coarsening/globularization [16]. Meanwhile, α→β transformation can dynamically occur [17,18] along with the concurrent rotation of the α platelets toward soft orientation [19]. All of these factors would give rise to flow softening and, hence, promote strain localization [7,20]. Moreover, it is known that the flow strength of the α-phase is considerably higher than that of β; it behaves as a dispersion of hard inclusions, and the deformation can be concentrated in the softer β-matrix [2,21]. This, as well as the strong deformation compatibility at the α/β interface, can promote the refinement of the β-phase in local regions, but evident deformation/microstructure inhomogeneity is generally accompanied [21].

Indeed, it is challenging to achieve a refined and homogenous grain structure solely by hot working. However, static/metadynamic recrystallization (MDRX) occurs quite rapidly during the interpass or post-deformation annealing [22]. A multi-pass deformation–annealing sequence could be properly designed to achieve the best ingot breakdown effect. It has been widely accepted that the primary hot working of the titanium alloys involves β-working performed at ~150 °C above the β-transus, followed by α/β-working conducted at ~50 °C below the β-transus [23]. Owing to the low deformation resistance and the superior workability of the β-phase at an elevated temperature, the first working step can convert the initially coarse and textured microstructure into a fine and homogenous β grain matrix [6,7], which is particularly necessary for the near-β titanium alloy to reduce the chemical segregation [1]. The subsequent hot-working step is required to adjust the microstructure through spheroidization/precipitation of the lamellar α, whereby a bi- or tri-modal structure can be obtained for secondary mill processing [1,7]. After the primary hot working, an additional deformation at ~50 °C above the β-transus is necessary for further improvement in the grain structure [23]. This gives rise to a regular "high–low–high" primary hot-working sequence, especially for near-β titanium alloys [12,14]. However, the origin of the significance and necessity has not been systematically clarified for such a working sequence.

As aforementioned, there have been a great number of studies concerning the flow behavior and microstructural conversion mechanism of near-β titanium alloys during hot deformation. However, most of them were focused on individual hot-working steps. The effect of complicated thermomechanical cycles seems to be paid less attention. Moreover, they were generally conducted on laboratory-scale ingots or as-forged alloys with small β grain sizes, which were far different from the engineering reality. To this end, the present work aims to study the macro- and micro-structure evolution during multi-step hot working of a typical near-β titanium alloy, i.e., ton-scale Ti-55511 (Ti-5Al-5V-5Mo-1Cr-1Fe in wt. %) ingot material with ultra-large β grain size. A comprehensive explanation of the microstructural conversion mechanism was proposed based on an orientation-driven perspective.

2. Materials and Methods

The as-cast Ti-55511 ingot with a dimension of Φ 690 mm × 3000 mm (weighed about 5 tons) was produced in Western Superconducting Technologies Co., Ltd. Xi'an, China, by means of vacuum arc remelting three times. The measured chemical compositions in different parts of the ingot are listed in Table 1. The β-transus was about 865–870 °C, which was evaluated by the metallographic method.

Table 1. Chemical composition of the Ti-55511 ingot (wt.%).

	Ti	Al	Mo	V	Cr	Fe	Zr	Si	C	H	O	N
Top	Bal.	5.29	5.03	5.12	1.120	0.945	<0.01	0.014	0.008	<0.001	0.113	0.014
Middle	Bal.	5.3	5.03	5.13	1.100	0.996	-	-	-	-	-	-
Bottom	Bal.	5.27	5.05	5.12	1.130	0.987	<0.01	0.014	0.008	-	0.11	0.014

For reproducing the primary hot-working sequences, cylindrical mults with dimensions of 100 mm × 200 mm were cut from the columnar grain zone, with their axes parallel to the prior ingot. Then, the mults were subject to multi-pass forging in a 630-ton hot/superplastic forming machine. To simplify the situation, a persistent uniaxial upsetting was applied instead of the complicated upsetting–cogging technology. Eight series of processing sequences were designed, as depicted in Figure 1. The mults were preheated to the target temperature in a muffle furnace and soaked for 2 h to homogenize the temperature. After that, they were transferred into the forming machine and compressed by a height reduction of 40% for each pass. That is, in the first pass, the height was reduced from 200 mm to 120 mm and 72 mm in the second pass, while the target height of the third pass was ~43 mm. After each intermediate upsetting pass, the workpiece was air-cooled to room temperature and reheated up to the target upsetting temperature for another 2 h soaking. Since the workpieces were much smaller in comparison with the parent ingot, the working chamber of the forming machine was preheated up to ~700 °C to reduce the heat loss. A constant upsetting speed of ~2 mm/s was applied, which corresponded to a true strain rate from 0.01 s^{-1} up to ~0.05 s^{-1}. After the last processing step, all the workpieces were water-quenched to room temperature to preserve the high-temperature microstructure. Moreover, to reveal the microstructure evolution behavior during post-deformation annealing, additional short-term heat treatments were conducted on small specimens machined from the workpieces.

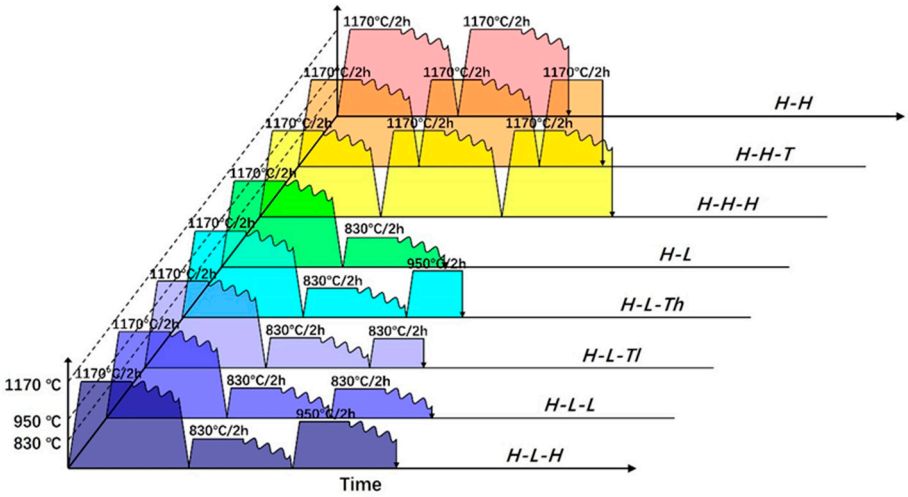


Figure 1. Schematic diagrams of the applied multi-pass upsetting routes for primary hot working of Ti-55511 alloy. H denotes the upsetting temperature higher than β-transus, while L denotes the lower upsetting temperature. T and Th represent the annealing temperature higher than β-transus, and Tl represents lower annealing temperature.

The workpieces were sectioned along the central axis after processing. The cross-sections were mechanically ground and etched using Kroll solution (10% nitric acid + 10% hydrofluoric acid + 80% water). Owing to the ultra-large grains, the macrostructure was captured using a camera, whereby the grain size distribution could be evaluated by the line-intercept method. However, one should note that this is rather a rough estimation since the LAGBs (low-angle GBs) cannot be differentiated from the HAGBs in the photographs. Furthermore, apparent microstructural information was presented by optical microscopy (OM).

To reveal the evolution of microstructure and texture, EBSD (electron back-scattered diffraction) was carried out on a Zeiss-Sigma500 scanning electron microscope (SEM) equipped with Channel 5 software. For this purpose, specimens were cut from the representative regions of the workpieces and subsequently subjected to mechanical grinding, followed by polishing using a mixture of colloidal silica and hydrogen peroxide. The EBSD was performed under an acceleration voltage of 20 kV. In consideration of the ultra-large β grains, a stepping size of 5 μm was applied, and the scanning area reached ~0.5 square centimeters to cover sufficient microstructural details. For texture analysis, ultra-large areas (1~2 square centimeters) were scanned in the center region of the workpieces under a stepping size of 5–20 μm. The textures were analyzed using ATEX software. Specifically, a small stepping size of 1 μm was also applied to characterize microstructural details in highly misoriented regions. It should be mentioned that due to the strain-induced α→β transformation below the β-transus, the volume fraction of the α-phase is negligible (~1%) with a disproportionate grain size to that of the β-matrix. Therefore, the α-phase is ignored during EBSD mapping. It has little influence on the present study since the β grain refinement is the primary concern. Emphasis was placed on the crystalline misorientation. Therefore, GBs were identified and classified based on the misorientation. The LAGBs or sub-GBs were those with misorientations in the range of 2–15°, while others were recognized as HAGBs.

3. Results

3.1. As-Cast Material

The macro- and micro-structures of the ingot material are shown in Figure 2. As expected, the ingot is characterized by three different zones from surface to inner, namely, the fine-grained chill zone, the columnar grain zone, and the equiaxed grain zone. Meanwhile, the prior grains are extremely large due to the low cooling rate of such a large ingot. Even in the chill zone, a mean size of ~7.3 mm is noticed. Figure 2b suggests that the alloy is characterized by a transformed structure mainly consisting of coarse and basketweave α lamellae, while the prior β-GBs can be readily distinguished owing to the precipitation of continuous α layers as well as the Widmannstätten colonies growing from them.

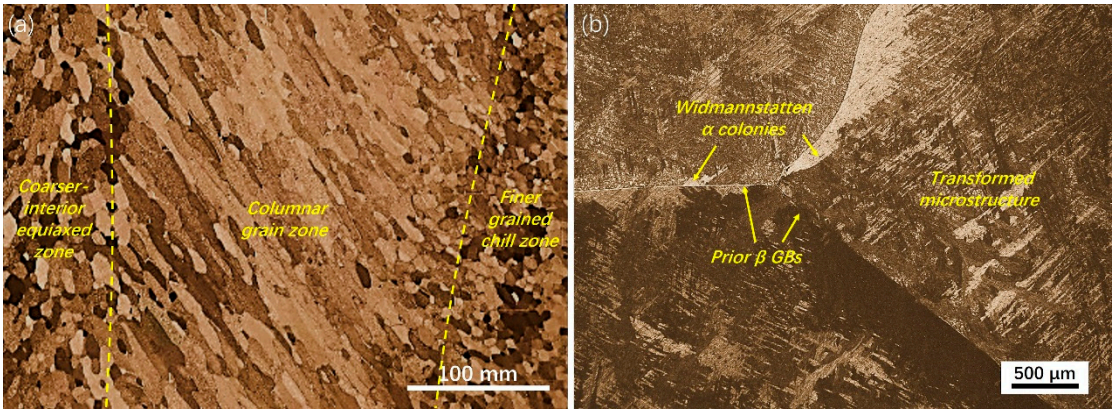


Figure 2. (**a**) Macrostructure and (**b**) Microstructure of the ton-scale Ti-55511 ingot material.

3.2. Apparent Macrostructure Characterization

3.2.1. Two-Pass Upsetting

As schematically described in Figure 1, there are two workpieces processed by two-pass upsetting routes, i.e., H-H and H-L, to characterize the intermediate structure evolution. As shown in Figure 3a, a two-pass upsetting at 1170 °C (H-H) results in a nonuniform structure, which is manifested by the presence of dead-metal zones (outlined by dash lines) and noticeable bulges. This is a typical metal flow defect during the upsetting of cylindrical mults and is mainly caused by die chilling and friction [20]. As a consequence, the β grains within the dead metal zones, which are globularized by the previous thermomechanical cycle, are slightly deformed. Meanwhile, the strain concentration in the center region of the workpiece leads to apparent flattened/elongated β grains. Given the fact that the deformation is dominated by DRV, the strain localization may be roughly estimated by a merely geometrical method. Assuming that the prior grain has a cubic shape with an edge length of L_0, it becomes $W \times W \times L$ after deformation, where W is the width of the flattened cube, and L is the thickness. By means of the uniform strain (Taylor) assumption [7], the true strain can be readily deduced as follows:

$$\varepsilon = -\ln\left(\frac{L}{L_0}\right) = -\ln\left[\frac{L}{(W^2L)^{1/3}}\right] = \frac{2}{3}\ln\left(\frac{W}{L}\right) = \frac{2}{3}\ln k, \quad (1)$$

where k is the width/thickness ratio of the grains, and a mean value of ~6 is measured at the center region of H-H. This corresponds to a true strain of ~1.2, while the nominal strain is only ~0.5 (i.e., 40% in height reduction) in the current upsetting stage. Remarkable strain localization arises.

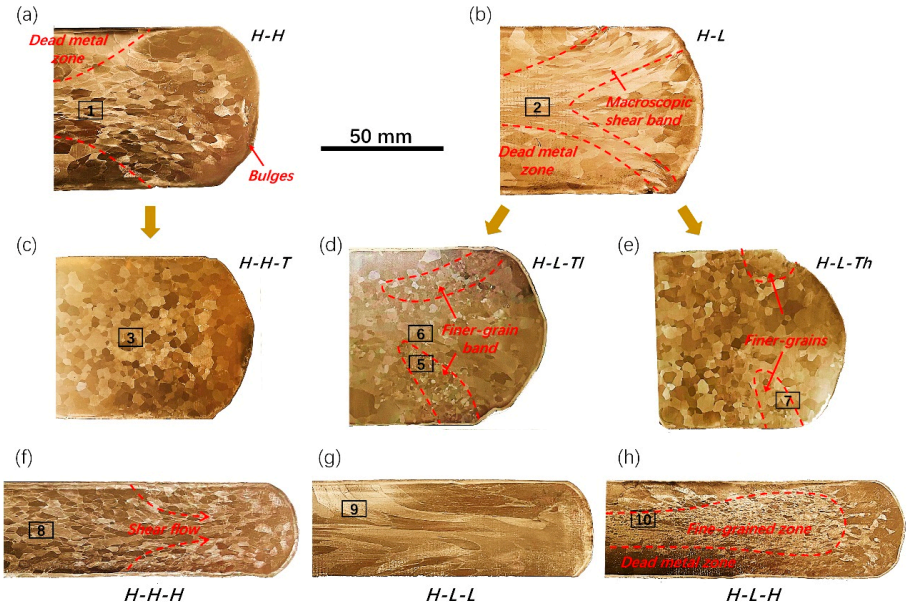


Figure 3. Macrostructures of the workpieces after various multi-pass hot working: (**a**) H-H; (**b**) H-L; (**c**) H-H-T; (**d**) H-L-Tl; (**e**) H-L-Th; (**f**) H-H-H; (**g**) H-L-L and (**h**) H-L-H. The regions marked with different numbers were analyzed in detail hereinafter.

The situation is even worse for the H-L workpiece. As shown in Figure 3b, the dead-metal zones are larger than in H-H, and the strain is highly localized so that an X-type macroscopic shear band is produced diagonally across the entire workpiece. The grains within the shear band are extremely elongated so a mean k value of ~40 is estimated, corresponding to a true strain of ~2.5 derived from Equation (1). Such a value is nearly twice the H-H value, indicating that α/β-working is detrimental to the homogeneity of deformation.

3.2.2. Post-Deformation Annealing

The microstructural inhomogeneity can be moderated by post-deformation annealing. The grain size distribution is fairly uniform in the H-H-T workpiece, see Figure 3c. An obvious refinement is achieved even in the prior dead-metal zones. The mean grain size is estimated to be ~3.3 mm, which is highly refined compared to the as-cast state. On the contrary, in the H-L-Tl, the grain size exhibits a bimodal distribution, as shown in Figure 3d. A much finer grain structure (~1.0 mm) is yielded within the prior shear band, whereas other regions display a coarser structure (~3.8 mm). Apart from that, the dead-metal zones are still evident after annealing. As for H-L-Th (Figure 3e), it confirms that elevating the annealing temperature up to the β-phase field can effectively increase the microstructural homogeneity, especially in the dead-metal zones. However, microstructural inhomogeneity still exists, as evidenced by the finer grains in the corner regions of the workpiece. An overall grain size of ~3.4 mm is obtained, which is slightly lower than that in H-H-T.

The homogeneity of grain structure is quantitatively analyzed using grain size statistics along the axes of the workpieces. As demonstrated in Figure 4a, H-L-Th shows a similar distribution mode with the H-H-T, and the curve slightly shifts toward a smaller size value owing to the lower annealing temperature. Meanwhile, the bulk of H-L-Tl possesses a much smaller grain size, but the grains in dead-metal zones are excessively large, which is even comparable to that in H-H-T. The error margin for H-L-Tl reflects a strong polarization of grain size in the dead-metal zones, implying that the recrystallization only partially occurs during annealing at 830 °C. Given the fact that the starting material for H-L-Tl and H-L-Th is identical, it can be concluded that the recrystallization is much more sluggish in the dual-phase region.

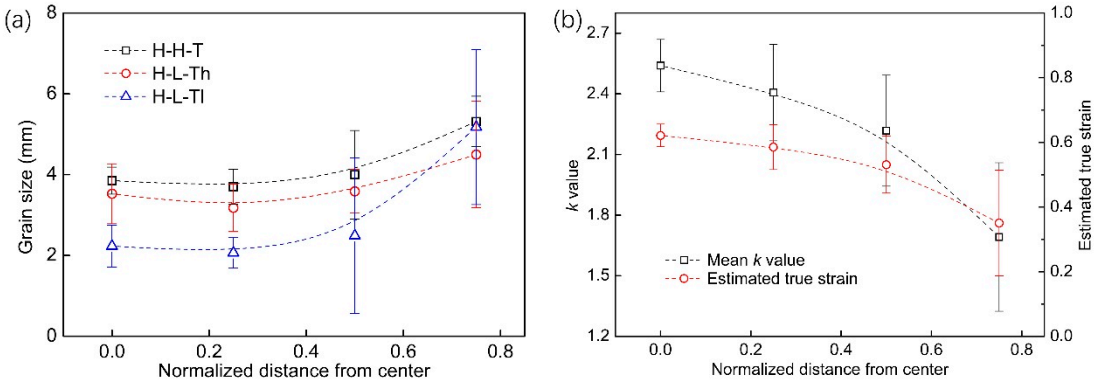


Figure 4. (**a**) Grain size distribution along the center axis of the three annealed workpieces. (**b**) The distribution of the k value along the center axis and the corresponding true strain for H-H-H.

3.2.3. Three-Pass Upsetting

After the third-pass upsetting, the three workpieces exhibit thoroughly different morphologies. As shown in Figure 3f, it is strange to notice that the macrostructure of H-H-H appears to be fairly uniform, and the dead-metal zones seem absent. The distribution of the grain width/thickness ratio (k) along the central axis is depicted in Figure 4b, together with the corresponding true strain derived from Equation (1). Noticeably, the maximum true strain, ~0.62, is close to the nominal strain (~0.5). Even for the dead-metal zones, a true strain of ~0.35 is evaluated. Such an abrupt macrostructural homogeneity compared to that in H-H, however, seems unreasonable since the deformation nonuniformity is inevitable during a non-isothermal upsetting. Some mechanisms have to be responsible for it and will be analyzed later. Nevertheless, the trace of shear flow can be faintly recognized, as indicated in Figure 3f, which indicates a nonuniform metal flow.

For the H-L-L workpiece, as shown in Figure 3g, it is not surprising that all the grains are as elongated as that in H-L. No apparent macrostructural refinement can be noted, and a fibrous macrostructural morphology is produced instead. An interesting macrostructure is observed in H-L-H. Remarkably, the bulk of the workpiece seems to be drastically refined,

while the dead-metal zones are quite prominent, with grain sizes comparable to that in H-L-Th. Such a sharp contrast seems contradictory to the preconceived assumption that the β-working is able to yield a homogeneous microstructure, as that in Figure 3f. Anyway, the existence of the dead-metal zones indicates intensive strain localization in the center region, and the resulting high stored deformation energy is thought to be the primary reason for the formation of the fine-grained zone outlined in Figure 3h.

According to the results presented above, one may conclude that when the primary hot working is performed at ultra-high temperature (far higher than β-transus), uniform deformation and microstructure can be achieved. Even the dead-metal zones can be seemingly eliminated. However, the obtained grain size is relatively coarse. Persistent subtransus upsetting results in severe strain localization and microstructural inhomogeneity. It cannot effectively break down the as-cast microstructure, even though recrystallization can be initiated during post-deformation annealing. A combination of high–low–high upsetting sequences can remarkably refine the microstructure, while the dead-metal zones are strikingly evident. The underlying mechanism governing such significant differences will be analyzed and discussed later.

3.3. Microstructural Evolution

3.3.1. β-Working

In order to reveal the microstructure and orientation evolution, inverse-pole-figure (IPF) maps projecting in the upsetting direction (U.D.) are employed. The GBs are also superimposed on the IPF maps to characterize the local misorientation. Figure 5a,b shows the IPF maps for H-H, corresponding to the local regions 1, as indicated in Figure 3. At first glance, one can note that most deformed grains tend to arrange their <001> directions parallel to U.D., while a few grains exhibit a preferential orientation around <111>//U.D. Consequently, a strong <001> fiber is produced with a high pole density, as elucidated by the IPF shown in Figure 5c. In fact, this is anticipated since, in the case of body-centered cubic (BCC) metals, <001> + <111> orientations are stable for uniaxial compression, and the <001> fiber is generally stronger under hot compression [24–26].

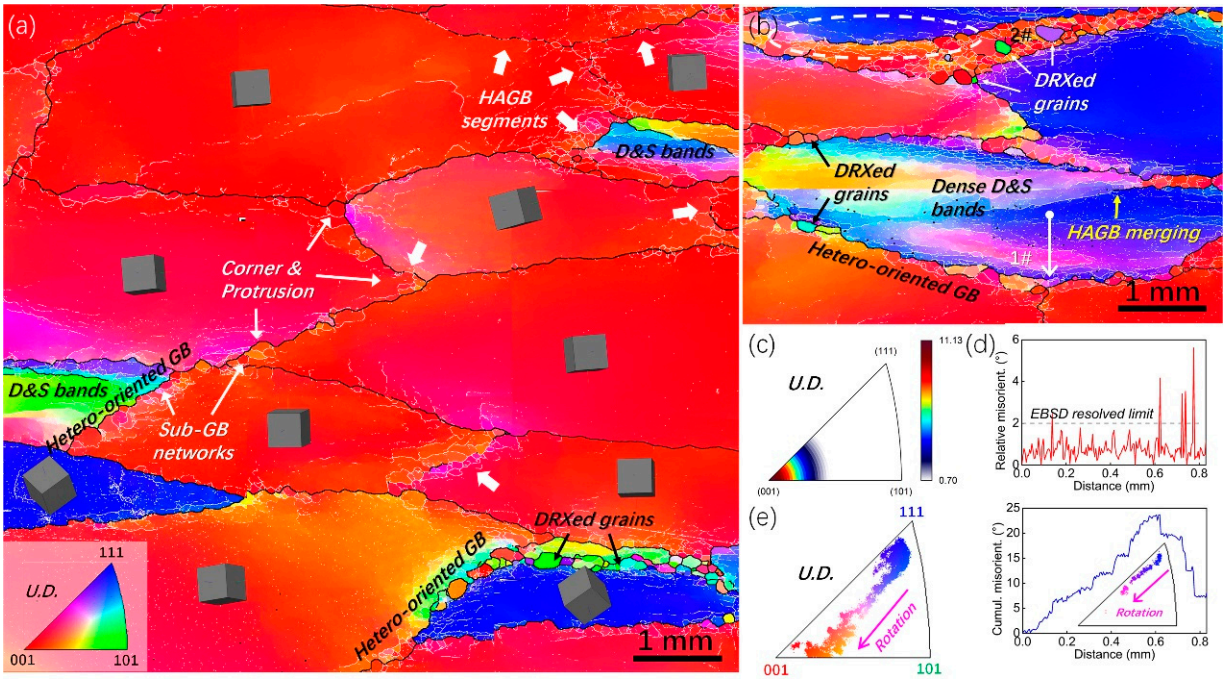


Figure 5. (**a**,**b**) IPF maps in region 1 of H-H (see Figure 3). (**c**) IPF for H-H in the center region. (**d**) The point-to-point and point-to-origin misorientation profile along line 1# in (**b**). (**e**) IPF map for the outlined region in (**b**).

Due to the large area fraction, the <001>-oriented grains are interlinked and border on each other. However, the flattened/elongated grain interior is deficient in substructures, except for some long and unevenly distributed LAGBs. Only in grain corners/protrusions can some well-developed sub-grains be produced, where the strain incompatibility is obviously large. The lack of substructures is probably related to the low stored energy owing to the lowest Taylor factor of <001> orientation [27]. Consequently, no evident DRX nuclei were noted in this large <001> grain area since DRX generally proceeds from microstructural inhomogeneities [10]. However, a distinct phenomenon should be noticed that the LAGBs in the grain interior tend to entangle together, trying to arrange themselves into HAGBs. This is clearly evidenced by the discontinuous HAGB segments embedded in the LAGB tangles, as indicated by thick arrows in Figure 5a. According to the morphologies of these incomplete HAGBs, one can clearly observe their gradual closing up, and the prior large grains are, thereby, fragmentized into smaller segments. Such a "LAGB merging" mechanism seems to be significant for the β grain breakdown at small height reductions.

The case is quite different for the <111>-oriented grains. Firstly, dense LAGBs are produced in the vicinity of the <111>-<001> hetero-orientated GBs, resulting in well-developed sub-GB networks and frequent DRX grains. Secondly, an intensive orientation gradient is noticed within the <111> grains, forming dense deformation/shear (D&S) bands enriched with sub-GB networks. A developing D&S band is labeled 1# in Figure 5b, and Figure 5d shows the corresponding misorientation profiles along the arrow. The variations in point-to-point misorientation reveal the presence of dense transverse LAGBs parallel to the band, while the cumulative orientation profile manifests a broad increase, followed by a decrease in misorientation with distance. The corresponding IPF clearly demonstrates the orientation transformation from <111> to <001>. Meanwhile, these parallel LAGBs try to merge into HAGBs, as indicated in Figure 5b, which yields definite band boundaries, as clearly shown in Figure 5a. A well-developed D&S band is labeled 2#, where a narrow <001> ribbon is embedded within a <111> grain. The discontinuous band boundaries demonstrate that the band is actually a part of the circumambient grain. Again, the local IPF (Figure 5e, corresponding to the outlined area) confirms a continuous orientation transformation from <111> to <001>. Owing to the pronounced strain localization, a well-developed sub-GB network with a mean size of less than 100 μm is formed within the band. However, these sub-grains are highly aligned to <001>, though DRX grains are occasionally produced.

Similar to H-H, the grains in H-H-H and H-L-H also exhibit <001> and <111> preferential orientations, as demonstrated in Figure 6. However, the proportion of <111> grain is evidently increased, as elucidated in Figure 6c,d. This is consistent with other studies that the <111> texture component can be strengthened by decreasing temperature and/or increasing strain rate in BCC alloys [25,26]. Furthermore, the LAGB merging in <001> grains is activated more vigorously. A HAGB network gradually emerges as a consequence, leading to the formation of numerous GB triple-points (indicated by dash cycles) as well as the dramatical fragmentation of the parent β grains. A prominent example is shown in Figure 6a, where three explicit GBs labeled B1, B2, and B3 are presented. Although B3 is a HAGB with a misorientation of 21–23°, it has to be formed during deformation since a prior HAGB cannot terminate in the grain interior. Meanwhile, the developing HAGB B2 and the LAGB B1 have a misorientation angle of 12–15° and 8–9°, respectively. The conservation of the misorientation (B1 + B2 = B3) confirms that these GBs are produced via dislocation accumulation followed by LAGB merging [28,29]. In addition, the newly formed GB networks always connect the grain corners/protrusions where the strain incompatibility is remarkable. Therefore, one may further speculate that the formation of the GBs is driven by the heterogeneous stress concentration [30]. The intensive LAGB merging, which may be stimulated by the higher strain rate and/or lower temperature, is thought to be the exact reason responsible for the homogeneous macrostructure in H-H-H (Figure 3f), as well as the excessively low k values. However, the density of the substructures within the <001> grain area remains at a low level.

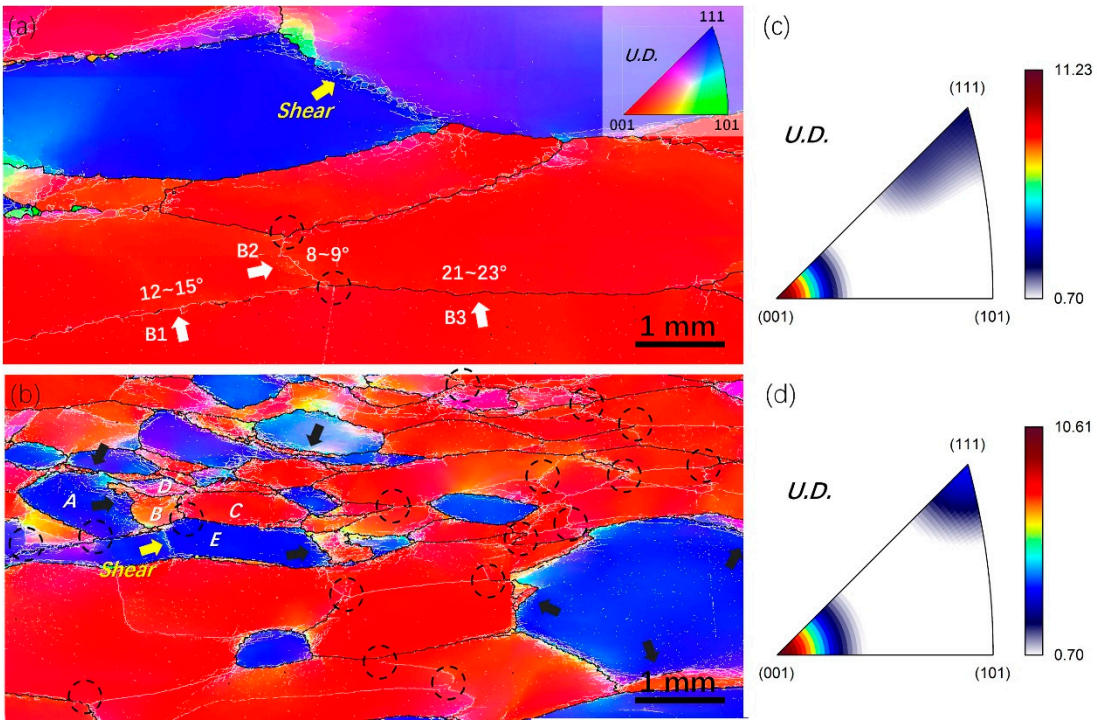


Figure 6. IPF maps showing the microstructure in regions 8 and 10 (see Figure 3) of (**a**) H-H-H and (**b**) H-L-H. (**c**,**d**) IPF of H-H-H and H-L-H, respectively.

Owing to the relatively large number of <111> grains in H-H-H and H-L-H, D&S bands are widely distributed with a preferential orientation toward <001>. Meanwhile, the D&S bands exhibit ribbon-like morphology. As indicated in Figure 6b, though area B is <001>-orientated with definite HAGBs, it has to be strain-induced since regions A–E are actually interconnected. The circumambient HAGBs in these areas have complex curvatures, indicating the occurrence of GB migration and, hence, the irregular inflation of the D&S bands. Other plausible D&S bands are indicated by dark arrows. Moreover, occasionally, large <111> grains can split by producing GBs (yellow arrows), analogous to the LAGB merging mechanism mentioned above. However, these GBs seem to be shear-induced since they are always oblique to the upsetting axis and accompanied by severe crystalline distortion. Nevertheless, it plays a minor role in the breakdown of the <111> grains.

In conclusion, a moderate β-working results in the orientations highly around <001>, as well as a weak convergence to <111>. The <001> grains are mainly fragmentized via a LAGB merging mechanism, while the breakdown of the <111>-oriented grains is predominated by D&S bands. DRX is found to occur within D&S bands and in the vicinity of the <111>-<001> hetero-oriented GBs. However, it plays an insignificant role in grain refinement due to the negligible volume fraction.

3.3.2. α/β-Working

Subtransus working also results in a <001> + <111> preferential orientation, whereas the <111> becomes predominant instead. The maximum pole density is located at <111> with a value of ~10, as shown in Figure 7a–c. This is consistent with the variation in texture in H-H-H and H-L-H compared with H-H. The <111> texture component was strengthened as the temperature decreased. The texture evolution during hot compression of BCC alloys was generally controlled by temperature and strain rate, and the DRX was considered the main reason. The <001>-oriented grains are extremely flattened/elongated, but the LAGBs are seldom observed in the interior, and the LAGB merging is absent. This may be attributed to the retarded DRV caused by the lower temperature [24]. In contrast, severe

D&S bands can be noted in the <111> grains. Due to the drastic strain concentration, these bands are much smaller in width. Fine sub-grain structure and DRX grains are produced with randomized orientations (see Figure 7d). In addition, the formation of D&S bands is much more intense in the macroscopic shear regions of the workpieces. Hence, the DRX grains and shear-induced substructures are densely produced, as manifested in Figure 7b–e.

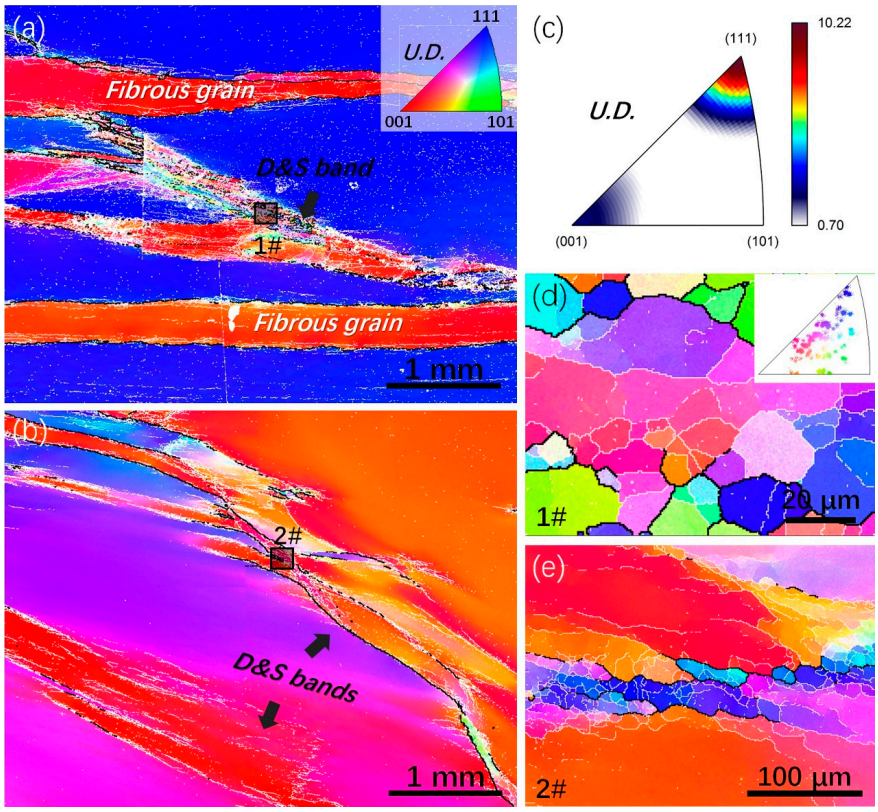


Figure 7. (**a**) Microstructure and (**c**) IPF of region 2 in H-L (see Figure 3). (**b**) Microstructure in the shear flow region 9 of H-L-L. (**d**,**e**) Microstructural details in areas 1# and 2#, respectively.

In conclusion, an α/β-working gives rise to rather sluggish DRV activity, whereby grain fragmentation is significantly retarded. While the stable <001> grains can hardly break down due to the absence of LAGB merging, the heterogeneously distributed D&S bands seem to be the only fragmenting mechanism for the <111>-oriented grains. As a consequence, the prior β grains are extremely flattened/elongated, and a fibrous morphology is produced.

3.3.3. Post-Deformation Annealing

In Section 3.2, it is concluded that post-deformation annealing gives rise to a thorough improvement in the deformed microstructure. It is confirmed by the IPF maps shown in Figure 8. H-H-T exhibits the most homogeneous grain structure. The prior sub-GBs are completely eliminated, and the HAGBs exhibit a straight morphology. Apparently, this arises from the relatively uniform deformation in H-H and the high annealing temperature. Meanwhile, the deformation texture, i.e., the <001> fiber, is obviously moderated from 11 to 5, but the preferential orientation around <001> is still visible. The grain structure in H-L-Th and H-L-Tl is less homogeneous, especially for the latter. In the macroscopic shear region, a refined, fully recrystallized grain structure is noticeable, as shown in Figure 8e. However, the grain size is excessively large in the center region (Figure 8f), and GBs display a curved morphology. More distinctly, the sub-GBs have not been exhausted. All these phenomena reveal an incomplete recrystallization in the center region of the workpiece, in contrast to that in H-L-Th. Hence, one can deduce that not only the DRV but also the GB

migration is dramatically retarded in the dual-phase field. Meanwhile, for both H-L-Th and H-L-Tl, the texture components in their predecessor H-L, i.e., a strong <111> plus a weak <001> fiber, are altered into a single <001> fiber with a pole density of only ~3.5. Hence, the following three conclusions can be derived: firstly, recrystallization annealing is of significance for texture mitigation, as that in other BCC metallic materials [31]; secondly, the <001> is, indeed, the most stable orientation even during recrystallization annealing; thirdly, the recrystallization mechanism is irrelevant to the annealing phase field and the prior deformation state, given the fact that all the annealing texture is roughly the same.

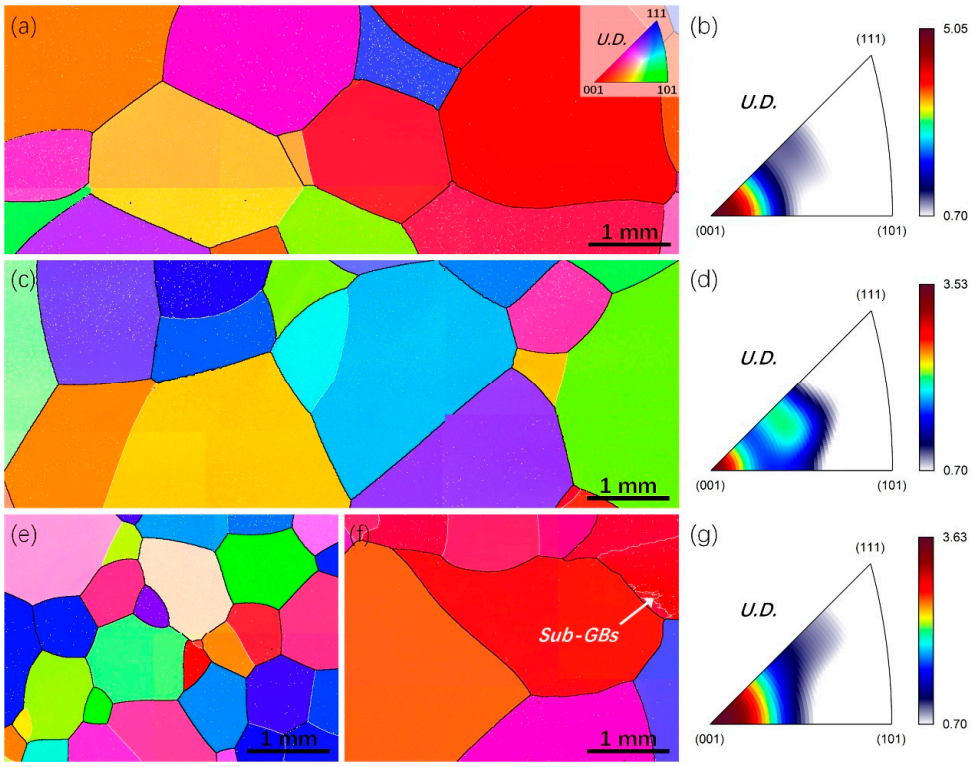


Figure 8. (**a**,**c**,**e**,**f**) Microstructures corresponding to regions 3,7,5,6 in Figure 3. (**b**,**d**,**g**) IPFs for H-H-T, H-H-Th and H-L-Tl in the center regions.

In order to reveal the recrystallization mechanism during post-deformation annealing, the H-H samples are soaked at 950 °C for various times, as shown in Figure 9. In comparison with H-H, the most conspicuous phenomenon is the nucleation and growth of the recrystallized grains in the vicinity of the hetero-oriented GBs, as elucidated by Figure 9a,b. This is not surprising because DRX grains also preferentially nucleate here. However, it should be emphasized that except for the small amount of pre-existing DRX grains, most recrystallized grains are likely to be newly formed during annealing. This speculation is based on the fact that the number density of the post-DRX grains is much higher than that of the DRX grains. Therefore, the annealing is likely to be predominant by SRX nucleated via GB bulging or sub-grain merging rather than the MDRX process. Other possible/potential SRX nuclei are indicated by arrows, which are characterized by smooth borders without orientation spread in the interior.

After 10 min soaking, the SRXed nuclei rapidly grow up, and a necklace structure is formed surrounding the deformed grains, which manifest themselves by the interior orientation gradient or spread. This demonstrates that the SRX proceeds quite rapidly, as also noted by other studies. Moreover, a considerable number of recrystallized grains show a <001> preferential orientation. When the SRX is nearly finished (Figure 9d), a <001> texture is, therefore, produced, which is analogous to that observed in Figure 6.

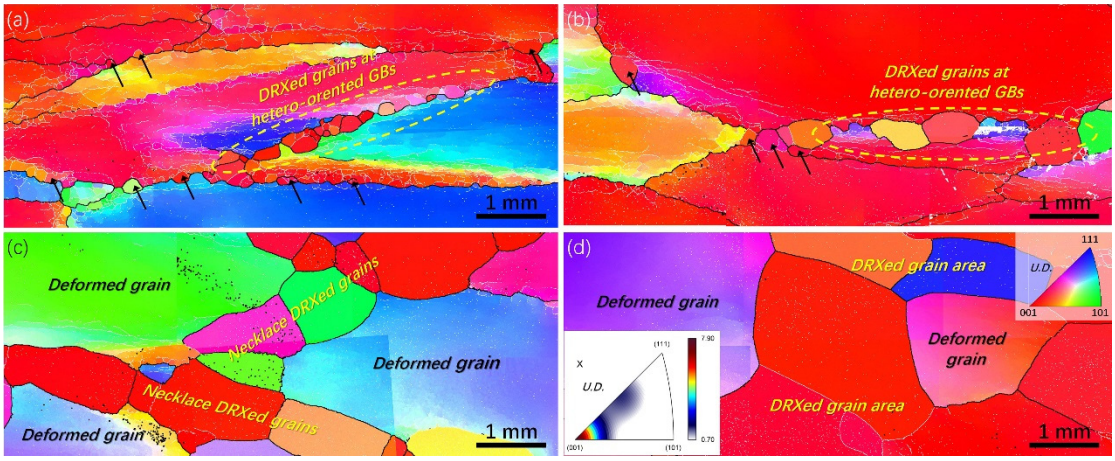


Figure 9. Microstructure evolution of H-H during annealing at 950 °C for: (**a**) 1 min; (**b**) 3 min; (**c**) 10 min and (**d**) 20 min.

In conclusion, a refined equiaxed grain structure can be achieved by recrystallization annealing either in the β-phase field or in the dual-phase field. The recrystallized kinetics, grain size, as well as microstructural homogeneity are closely related to the deformation state. Both MDRX and SRX contribute to the refinement, where the latter seems to be predominant. While the deformation texture is evidently mitigated and altered by recrystallization, the <001> preferential orientation is still evident after annealing.

4. Discussion

4.1. Deformation Nonuniformity

The most impressive observation with respect to the macrostructure is the deformation nonuniformity characterized by dead-metal zones and bulges. It shows that the nonuniformity seems weak when deformed at 1170 °C but becomes drastic at 830 °C and 950 °C, despite the same operating condition. Such a difference may be qualitatively clarified from the perspective of phase constituents. According to the related literature, one can summarize that the β-phase exhibits an almost steady-state flow under isothermal compression [9,10]. The apparent deformation activation energy (Q_{app}) is in the range of 130–200 kJ/mol, which is close to the activation energy for self-diffusion in the β-phase (~153 kJ/mol) [7]. In contrast, noticeable flow softening can be observed when deformed within the (α+β) dual-phase field. More importantly, due to the variations in the phase fractions with temperature, it yields a much higher Q_{app} value in the range of 400–700 kJ mol. Since the Q_{app} is derived from the partial derivative of ln(σ) (or ln[sinh($\alpha\sigma$)], where σ is the stress), with respect to $1/T$, a higher Q_{app} means that the flow stress is more sensitive to temperature change. Hence, the strain localization tendency is exacerbated during α/β-working, while it can be significantly moderated in the single β-phase field.

To further clarify the point, the finite-element method (FEM) is applied to model the temperature and strain evolution during the third upsetting pass. A simplified constitutive equation is developed based on the hyperbolic-sine law using the flow data in Ref. [31]. To ensure the continuity of the flow strength across the β-transus, the transient strain-hardening (deformation of dual-phase) and discontinuous yielding (deformation of β-phase) stage is ignored. While the flow stress of the β-phase is considered to be constant, the flow softening of the dual-phase is addressed by the method proposed by Laasraoui and Jonas [32,33], i.e., the apparent softening kinetics can be described by the JMAK-type equation. The developed model is as follows:

$$\begin{cases} \sigma = \sigma_p - X(\sigma_p - \sigma_s) \\ \sigma = \frac{1}{0.01} a\sinh\left[\left(\frac{Z_s}{1.52\times10^6}\right)^{1/3.7}\right] \\ X = 1 - \exp(-6.5\varepsilon^{1.26}) \\ \sigma_p = \frac{1}{0.0058} a\sinh\left[\left(\frac{Z_p}{5.86\times10^{22}}\right)^{1/3.83}\right] \\ \sigma_s = \frac{1}{0.0058} a\sinh\left[\left(\frac{Z_s}{1.46\times10^7}\right)^{1/4.6}\right] \\ Z_p = \dot{\varepsilon}\exp\left(\frac{494000}{RT}\right) \\ Z_s = \dot{\varepsilon}\exp\left(\frac{153000}{RT}\right) \end{cases} \quad (2)$$

For detailed annotation of the constitutive equation, one may refer to Appendix A. For verification of the constitutive model, the predicted true stress–strain curves, as well as flow kinetics, are compared with the flow data [31,32] applied for model development. As shown in Figure 10, the developed model can accurately reproduce the experimental results. For simulation of the hot-upsetting in the present study, the thermo-physical parameters for Ti-55511 alloy are adopted from Ref. [34], and the interface heat transfer coefficient is set to 11×10^3 W/m^2/K, with a friction coefficient of 0.5. The initial geometry of the workpiece is extracted from the profile of H-H (Figure 3a).

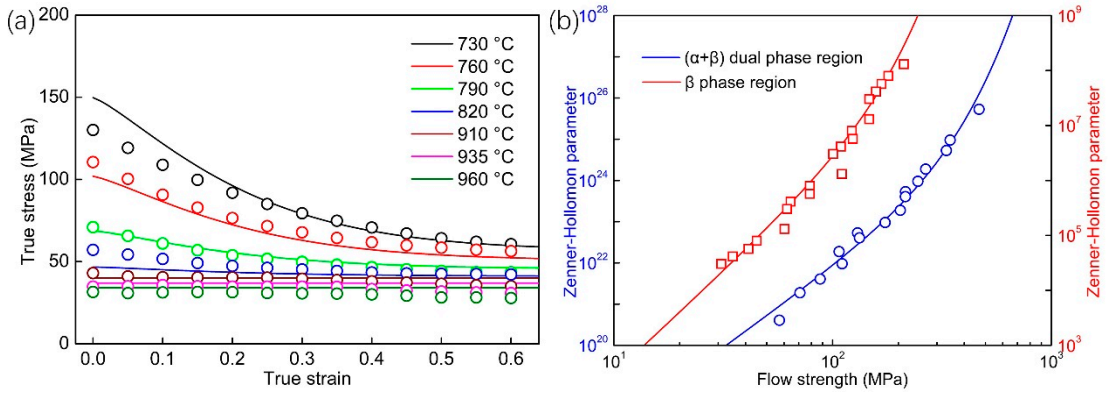


Figure 10. Comparison between the experimental data (symbols quoted from [31,32]) and the predicted results by the constitutive model (lines): (**a**) true stress – strain date at different temperatures and (**b**) the relationship between Zenner-Hollomon parameters and flow strength in (α + β) and β phase regions.

As shown in Figure 11, when the upsetting is performed at 1170 °C, the temperature of the workpiece is consistently above the β-transus despite the die chilling. The maximum and minimum equivalent plastic strains are ~1 and ~0.01, respectively. Comparing the strain contour with the macrostructure shown in Figure 3f, it can be speculated that a true strain below 0.1 is sufficient to trigger the LAGB merging mechanism in the dead-metal zones and lead to a uniform macrostructure. When the upsetting is conducted in a dual-phase field, as shown in Figure 6, drastic strain localization concentrated in an X-shape shear band was produced, analogous to that in H-L (Figure 3b). The maximum strain is as high as ~1.8, while the lowest value (~0.04) is only ~1/3 of that at 1170 °C. As for the case at 950 °C, the strain contour is rather similar to that at 1170 °C. However, the temperature drop leads to the variation in phase field in the contact surface regions, as indicated in Figure 11c. By superimposing the 870 °C iso-contour lines on the strain map (Figure 11f), one can clearly observe that the finer-grain region in Figure 3h is located at the intersection of a single β-phase and a relatively high strain (>0.6). Therefore, the abrupt dead-metal zones in H-L-H are caused by the change in the phase field. The LAGB merging mechanism cannot be initiated in the dead-metal zone, while its vigorous activity leads to the seemingly refined macrostructure in the center of the workpiece.

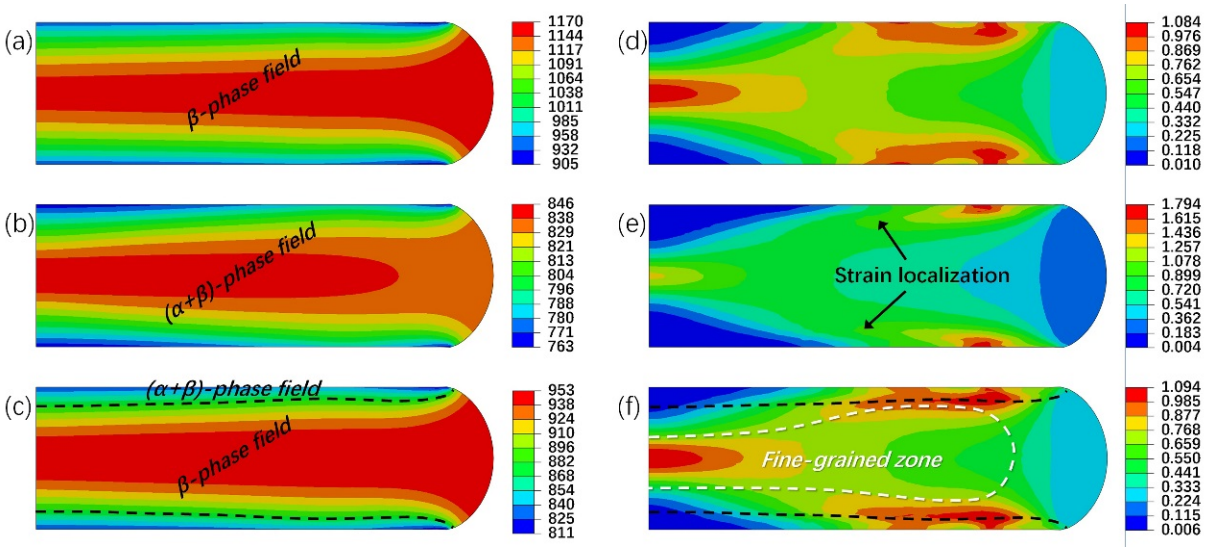


Figure 11. FEM prediction of (**a**–**c**) temperature distribution and (**d**–**e**) equivalent plastic strain distribution for (**a**,**d**) H-H-H, (**b**,**e**) H-L-L, and (**c**,**f**) H-L-H.

4.2. Microstructural Conversion Mechanism

One of the major concerns in primary hot working is efficiently refining the grains to the smallest possible size. However, the DRX is difficult to initiate in β-phase owing to the strong DRV tendency. This study suggests that the refinement of the ultra-coarse β grains is primarily achieved by SRX during post-deformation annealing. According to classical theory [35], the recrystallized grain size depends exponentially on the nucleation rate, which is correlated to the density of nucleation sites. Meanwhile, SRX always nucleates in regions with high local misorientations [36]. Therefore, the grain refinement effect, as well as the homogeneity, is primarily decided by the deformed state of the material. The present study clearly reveals the distinct differences in the deformation behavior and microstructural characteristics between β-working and α/β-working.

Upsetting above the β-transus results in a vast area of <001> grains, and D&S bands are massively formed in the <111> grains. With the ongoing straining, the LAGB merging gives rise to well-defined <001>-oriented D&S bands with explicit band boundaries. The preferential migration of these <001>-orientated boundaries leads to rapid expansion of the <001> grain area and the concurrent shrinkage of the <111> grain region. Therefore, the predominance of the <001> grains at β-working can be attributed to a deformation-induced <111>→<001> orientation transformation and the preferential migration of the <001>-oriented GBs. This is essentially attributed to the high stability against deformation of the <001> oriented grains with the lowest Taylor factor [24]. Due to the same reason, the substructures are rarely observed in the vast <001> grain area. Instead, the <001> grains are fragmentized via LAGB merging. However, such a mechanism is difficult to label as a CDRX process since no stable sub-GB network has been produced as a prerequisite [36].

When an α/β-upsetting is conducted, the grains prefer to align to <111> rather than <001> due to the retarded DRV, as well as the sluggish GB migration facilitated by the precipitation of GB α. The deficiency of the restoration mechanisms causes the extremely elongated/flattened <001> grains without evident fragmentation. Meanwhile, the <111> grains are characterized by strong strain localization, leading to highly misoriented D&S bands with random-oriented fine (sub-) grains.

The SRX always proceeds from microstructural inhomogeneity and preferentially nucleates at highly misoriented regions. Therefore, when the β-worked material is subject to annealing, the nucleation is mainly located in the vicinity of <001>-<111> hetero-oriented GBs or band boundaries. Due to the minimized <111> grain number, especially at high temperatures and low strain rates, the hetero-oriented GBs are hardly observed (Figure 5a). Although the developing D&S bands are enriched in subgrains (Figure 5b), these grains preferentially align to <001> and, hence, are difficult to evolve into highly active nuclei. Therefore, the density of the SRX nucleation sites is quite low in β-worked material, leading to inefficient SRX kinetics as well as a coarser grain size. Again, the superior growth rate of the <001> nuclei allows them to predominate the SRX process. Thus, the <001> fiber is retained in the recrystallized microstructure. Nevertheless, the developing SRXed nuclei fronts would continuously consume the substructures, whereby the orientations can deviate from the parent <001> grains [24]. It accounts for the moderated texture strength after annealing.

As for the α/β-worked material, it is readily assumed that the SRX is initiated at the highly misoriented D&S bands in <111> grains. It is supported by the fact that the recrystallized grain size is much smaller within the prior macroscopic shear regions (Figure 8e,f). Therefore, the density of SRX nucleation sites is closely relevant to that of the D&S bands. Moreover, since the substructures within the bands are significantly randomized in comparison with those under β-working, the ultimate <001> texture can be moderated further.

4.3. Implications for Efficient Ingot Breakdown

According to the above analysis, one may summarize that the ingot-breakdown effect for Ti-55511 alloy is fundamentally determined by the competition between <001>- and <111>-oriented grains: (i) The <001>-oriented grains, as the most stable orientation under hot-compression due to the lowest Taylor factor, are barely prone to strain localization neither in β- nor in the dual-phase field. The predominance of them is beneficial for deformation uniformity but contributes rare nucleation sites for subsequent SRX; (ii) The <111>-orientated grains, which possess the largest Taylor factor [27], are highly inclined to heterogeneous deformation. Dense D&S bands with high misorientations are produced, especially in the macroscopic shear bands. Numerous SRX nucleation sites are, therefore, provided, which is favorable for SRX. The proportion ratio between <001> and <111> grains is determined by the deformation temperature and strain rate. An appropriate combination of β- and α/β-working is, therefore, the most effective approach for primary hot working of the near-β titanium alloys. That is, an α/β-working can be utilized to produce dense nucleation sites for SRX, while the β-working (annealing) is able to homogenize the macro-/micro-structure. To be more clear, during β-working the <111>→<001> orientation transformation should be reduced, while more microscopic D&S bands can be introduced at α/β-working.

For this purpose, a higher die speed may be recommended for both the β-working and α/β-working in the commercial production of Ti-55511. From the macroscale aspect, a high forging rate reduces the overall time of deformation, preventing excessive heat loss and large thermal gradients in the workpieces [20]. According to the present study, it is particularly significant for deformation below or slightly above the β-transus. Thereby, the severe strain localization and macroscopic shear bands can be moderated. From a microscopic viewpoint, a higher strain rate can reduce the <111>→<001> transformation during β-working and promote the fragmentation of the <001> grain area. Hence, it is favorable to achieve a seemingly finer β-matrix. In the α/β-working, a higher strain rate plus a multi-axial upsetting–cogging could induce more microscopic D&S bands with various orientations. However, the forging temperature and the deformation per pass should be carefully designed to avoid shear cracking or macroscopic shear bands.

5. Conclusions

This work aimed to study the primary hot working behavior of a ton-scale Ti-55511 ingot material with ultra-coarse β grains. Emphasis was paid to the grain refinement mechanism and the structural homogeneity during various multi-pass deformations. The main conclusions are drawn below:

(1) When the hot working was performed far above the β-transus, the flow localization was significantly moderated. A seemingly uniform macrostructure can be obtained after two-pass uniaxial upsetting, even without obvious dead-metal zones. However, when the deformation temperature was slightly higher than β-transus, the temperature dropping at the two ends of the workpieces led to α/β-working, while drastic strain localization was caused in the center region. Subtransus upsetting resulted in severe deformation, nonuniformity, and even macroscale shear bands. The grains were extremely flattened/elongated without apparent fragmentation;

(2) The grains were highly aligned to <001> orientation after β-upsetting, while only a few <111> grains were retained. The <001>-orientated grains were prone to deform uniformly without massive formation of sub-GBs. Hence, their fragmentation was mainly achieved by a LAGB merge mechanism in β-working. LAGBs were produced via dislocation accumulation and then arranged into HAGBs. Meanwhile, the deformation-induced <111>→<001> orientation transformation was noted in <111> grains, leading to the formation of numerous <001>-oriented D&S bands. The preferential migration of the band boundaries accounted for the predominance of the large <001> grain area. In contrast, the α/β-working significantly strengthened the <111> orientation accompanied by the weakening of <001>. The retarded DRV and GB migration rendered fragmentation of the <001> grains, while severe strain localization occurred within the <111> grains with highly misoriented D&S bands;

(3) The grain refinement was accomplished by the SRX during post-deformation annealing. Elevating the annealing temperature above the β-transus can promote SRX and homogenize the grain structure. The SRX mainly nucleated within the highly misoriented regions, including the <001>-<111> hetero-oriented GBs and the severe D&B bands within the <111> grains. Due to the preferential growth of the <001> grains, the recrystallized texture was characterized by a weak <001> fiber, irrespective of the working/annealing phase field.

Author Contributions: Conceptualization, X.L.; methodology, X.L., T.W., L.C. and K.W.; formal analysis, T.W., X.R., J.F., L.C., B.Z. and K.W.; investigation, T.W., X.R., J.F., L.C. and B.Z.; data curation, T.W.; writing—original draft preparation, X.L. and T.W.; writing—review and editing, L.C., B.Z. and K.W.; funding acquisition, X.L. All authors have read and agreed to the published version of this manuscript.

Funding: This research was funded by the State Administration of Science, Technology, and Industry (No. JPPT-135-HX-010-1), the National Natural Science Foundation of China (No. 51905233), and the Science and Technology project of Changzhou (No. CQ20210088).

Data Availability Statement: The data that support the findings of this study are available from the corresponding author, Xianghong Liu, and Tao Wang, upon reasonable request.

Conflicts of Interest: Tao Wang, Xiaolong Ren, Jie Fu and Kaixuan Wang were employed by Western Superconducting Technologies Co., Ltd. The remaining authors declare that the research was conducted in the absence of any commercial or financial relationships that could be construed as a potential conflict of interest.

Appendix A

In the constitutive equation, the physical implications of the material parameters and variables are listed in Table A1.

Table A1. Physical implications of the material parameters and variables in Equation (2).

σ	Current Flow Stress
σ_P	Peak stress when deformed in dual-phase region
σ_S	Steady-state flow stress when deformed in dual-phase region
X	Flow softening fraction when deformed in dual-phase region [(a)]
Z_s	Zenner–Hollomon parameter for steady-state flow stress [(b)]
Z_P	Zenner–Hollomon parameter for peak stress in dual-phase field
ε	True strain
$\dot{\varepsilon}$	True strain rate

(a) Because the strain hardening stage is ignored in the model, the prior JMAK equation is simplified to $X = 1 - \exp(-k\varepsilon^n)$, where k and n are material constants;.(b) for deformation within the β-phase, the apparent deformation activation energy is set to be the same as the self-diffusion energy, 153 kJ/mol. Due to the deficient steady-flow stress data for dual-phase, the corresponding deformation activation energy is assumed to be the same as that of the β-phase.

References

1. Fanning, J.; Boyer, R.; Lutjering, G.; Albrecht, J. (Eds.) *Titanium 2003: Science and Technology*; Wiley-VCH: Hamburg, Germany, 2003; Volume 4, pp. 2643–2650.
2. Wang, J.; Zhao, Y.; Zhao, Q.; Lei, C.; Zhou, W.; Zeng, W. Comparison on impact toughness of high-strength metastable β titanium alloy with bimodal and lamellar microstructures. *Metals* **2022**, *12*, 271. [CrossRef]
3. Boyer, R.R. An overview on the use of titanium in the aerospace industry. *Mater. Sci. Eng. A* **1996**, *213*, 103–114. [CrossRef]
4. Zhang, X.; Li, J.; Tao, M.; Wan, J.; Chen, B. Electron Beam Welding and Post Heat Treatment of a New Near-Beta High-Strength Ti-4Al-5Mo-5V-5Cr-1Nb Alloy. *Metals* **2022**, *12*, 1396. [CrossRef]
5. Guo, L.G.; Fan, X.G.; Yu, G.F.; Yang, H. Microstructure control techniques in primary hot working of titanium alloy bars: A review. *Chin. J. Aeronaut.* **2016**, *29*, 30–40. [CrossRef]
6. Zhao, Q.Y.; Sun, Q.Y.; Xin, S.W.; Chen, Y.N.; Wu, C.; Wang, H.; Xu, J.W.; Wan, M.P.; Zeng, W.D.; Zhao, Y.Q. High-strength titanium alloys for aerospace engineering applications: A review on melting-forging process. *Mater. Sci. Eng. A* **2022**, *845*, 143260. [CrossRef]
7. Semiatin, S.L. An Overview of the thermomechanical processing of α/β titanium alloys: Current status and future research opportunities. *Metall. Mater. Trans. A* **2020**, *51*, 2593–2625. [CrossRef]
8. Shi, S.X.; Ge, J.Y.; Lin, Y.C.; Zhang, X.Y.; Zhou, K.C. High-temperature deformation behavior and recrystallization mechanism of a near beta titanium alloy Ti-55511 in β phase region. *Mater. Sci. Eng. A* **2022**, *847*, 143335. [CrossRef]
9. Li, M.; Huang, L.; Zhao, M.J.; Guo, S.Q.; Li, J.J. Hot deformation behavior and mechanism of a new metastable β titanium alloy Ti–6Cr–5Mo–5V–4Al in single phase region. *Mater. Sci. Eng. A* **2021**, *814*, 141231. [CrossRef]
10. Lin, Y.C.; Huang, J.; He, D.G.; Zhang, X.Y.; Wu, Q.; Wang, L.H.; Chen, C.; Zhou, K.C. Phase transformation and dynamic recrystallization behaviors in a Ti55511 titanium alloy during hot compression. *J. Alloys Compd.* **2019**, *795*, 471–482. [CrossRef]
11. Pallot, L.; Piot, D.; Desrayaud, C.; Montheillet, F.; Bénéteau, A. Traitement Thermomécanique de L'alliage Ti-17 Dans le Domaine Bêta. Matériaux 2010, Nantes, France, DVD Publication: 2010.
12. Fan, X.G.; Zhang, Y.; Gao, P.F.; Lei, Z.N.; Zhan, M. Deformation behavior and microstructure evolution during hot working of a coarse-grained Ti-5Al-5Mo-5V-3Cr-1Zr titanium alloy in beta phase field. *Mater. Sci. Eng. A* **2017**, *694*, 24–32. [CrossRef]
13. Callegari, B.; Oliveira, J.P.; Coelho, R.S.; Brito, P.P.; Schell, N.; Soldera, F.A.; Mücklich, F.; Sadik, M.I.; García, J.L.; Pinto, H.C. New insights into the microstructural evolution of Ti-5Al-5Mo-5V-3Cr alloy during hot working. *Mater. Charact.* **2020**, *162*, 110180. [CrossRef]
14. Wang, H.D.; Ge, J.Y.; Zhang, X.Y.; Chen, C.; Zhou, K.C. Investigation of the dynamic recovery and recrystallization of near-β titanium alloy Ti-55511 during two-pass hot compression. *Metals* **2021**, *11*, 359. [CrossRef]
15. Balachandran, S.; Kumar, S.; Banerjee, D. On recrystallization of the α and β phases in titanium alloys. *Acta Mater.* **2017**, *131*, 423–434. [CrossRef]
16. Li, L.; Luo, J.; Yan, J.J.; Li, M.Q. Dynamic globularization and restoration mechanism of Ti–5Al–2Sn–2Zr–4Mo–4Cr alloy during isothermal compression. *J. Alloys Compd.* **2015**, *622*, 174–183. [CrossRef]
17. Guo, B.Q.; Jonas, J.J. Dynamic transformation during the high temperature deformation of titanium alloys. *J. Alloys Compd.* **2021**, *884*, 161179. [CrossRef]
18. Flower, H.M. Microstructural development in relation to hot working of titanium alloys. *Mater. Sci. Technol.* **1990**, *6*, 1082–1092. [CrossRef]
19. CPark, H.; Kim, J.H.; Hyun, Y.T.; Yeom, J.T.; Reddy, N.S. The origins of flow softening during high-temperature deformation of a Ti–6Al–4V alloy with a lamellar microstructure. *J. Alloys Compd.* **2014**, *582*, 126–129. [CrossRef]

20. Semiatin, S.L.; Seetharaman, V.; Weiss, I. Hot workability of titanium and titanium aluminide alloys—An overview. *Mater. Sci. Eng. A* **1998**, *243*, 1–24. [CrossRef]
21. Li, L.; Li, M.Q.; Luo, J. Mechanism in the β phase evolution during hot deformation of Ti–5Al–2Sn–2Zr–4Mo–4Cr with a transformed microstructure. *Acta Mater.* **2015**, *94*, 36–45. [CrossRef]
22. Fan, X.G.; Yang, H.; Gao, P.F.; Zuo, R.; Lei, P.H. The role of dynamic and post dynamic recrystallization on microstructure refinement in primary working of a coarse grained two-phase titanium alloy. *J. Am. Acad. Dermatol.* **2016**, *234*, 290–299. [CrossRef]
23. Lütjering, G.; Williams, J.C. *Titanium*; Springer: Berlin/Heidelberg, Germany, 2007.
24. Meng, L.; Kitashima, T.; Tsuchiyama, T.; Watanabe, M. β-texture evolution of a near-β titanium alloy during cooling after forging in the β single-phase and (α+β) dual-phase regions. *Metall. Mater. Trans. A* **2021**, *52*, 303–315. [CrossRef]
25. Cheng, L.; Zhang, S.J.; Yang, G.; Kou, H.C.; Li, J.S. Hot tensile behavior of a TiAl alloy with a (β0+γ) microduplex microstructure prepared simply by heat treatments. *J. Alloys Compd.* **2021**, *875*, 160039. [CrossRef]
26. Li, K.; Yang, P. The formation of strong {100} texture by dynamic strain-induced boundary migration in hot compressed Ti-5Al-5Mo-5V-1Cr-1Fe alloy. *Metals* **2017**, *7*, 412. [CrossRef]
27. Rosenberg, J.M.; Piehler, H.R. Calculation of the Taylor factor and lattice rotations for bcc metals deforming by pencil glide. *Metall. Trans.* **1971**, *2*, 257–259. [CrossRef]
28. Cheng, L.; Zhu, B.; Yang, G.; Qiang, F.M.; Li, J.S. Insights into the abnormal flow softening of lamellar γ-TiAl alloys during hot-working: Experimental analysis and numerical simulation. *Mater. Sci. Eng. A* **2022**, *852*, 143695. [CrossRef]
29. Cheng, L.; Qiang, F.M.; Li, J.S.; Bouzy, E. Quantitative evaluation of the lamellar kinking&rotation on the flow softening of γ-TiAl-based alloys at elevated temperatures. *Mater. Lett.* **2021**, *290*, 129458.
30. Masuda, H.; Sato, E. Diffusional and dislocation accommodation mechanisms in superplastic materials. *Acta Mater.* **2020**, *197*, 235–252. [CrossRef]
31. Raabe, D.; Lücke, K. Rolling and annealing textures of BCC metals. *Mater. Sci. Forum* **1994**, *157–162*, 597–610. [CrossRef]
32. Laasraoui, A.; Jonas, J.J. Prediction of steel flow stresses at high temperatures and strain rates. *Metall. Trans. A* **1991**, *22*, 1545–1558. [CrossRef]
33. Bambach, M.; Sizova, I.; Bolz, S.; Weiß, S. Devising strain hardening models using Kocks–Mecking plots—A comparison of model development for titanium aluminides and case hardening steel. *Metals* **2016**, *6*, 204. [CrossRef]
34. Chen, T. The Study of Hot Deformation Behaviour and Numerical Simulation of Heat Treatment of TC18 Titanium Alloy. Master's Thesis, Harbin Institute of Technology, Harbin, China, 2013.
35. Gottstein, G. *Physical Foundations of Materials Science*; Springer: Berlin/Heidelberg, Germany, 2004.
36. Doherty, R.D.; Hughes, D.A.; Humphreys, F.J.; Jonas, J.J.; Jensen, D.J.; Kassner, M.E.; King, W.E.; McNelley, T.R.; McQueen, H.J.; Rollett, A.D. Current issues in recrystallization: A review. *Mater. Sci. Eng. A* **1997**, *238*, 219–274. [CrossRef]

Disclaimer/Publisher's Note: The statements, opinions and data contained in all publications are solely those of the individual author(s) and contributor(s) and not of MDPI and/or the editor(s). MDPI and/or the editor(s) disclaim responsibility for any injury to people or property resulting from any ideas, methods, instructions or products referred to in the content.